Study and mitigation of calibration error sources in a water vapor Raman lidar

Leslie David [1], Olivier Bock [1], Christian Thom [2], Pierre Bosser [3], and Jacques Pelon [4]

[1]IGN LAREG Univ Paris Diderot, Paris, France
[2]IGN LOEMI, Saint-Mandé, France
[3]ENSTA Bretagne, Lab-STICC, France
[4]CNRS IPSL LATMOS, Paris, France

Correspondence to: Leslie David (leslie.david@mines-ales.org)

Abstract. A detailed investigation of calibration variation sources in the instrumental part of the detection-fibered, water vapor Raman lidar, Rameau, is presented. This lidar has been developed by the Institut National de l'Information Géographique et Forestière (IGN) together with the Laboratoire Atmosphères, Milieux, Observations Spatiales (LATMOS) and aims at calibrating GNSS wet delay signals and thus at improving vertical positioning. Several measurements campaigns enabled
5   to validate the capacity of the instrument to retrieve high accuracy water vapor measurements. However, in order to insure a good stability, regular calibrations were necessary and led us to seek for instability sources in each sub-system of the instrument. The calibration variations are shown to be induced by fiber mode fluctuations and spatial non-uniformity of the photomultiplier photocathodes, and are responsible for significant calibration coefficient drifts. Such drifts are incompatible with
10 both the long term stability required for applications such as climatology and the absolute accuracy needed for wet path delay correction of GNSS signals. We show by means of experimental tests that variation sources can be mitigated by means of an optimization and re-design of the optical detection system, a careful alignment procedure, and the operational monitoring of the system with dedicated measurements. In order to validate the modifications of the system and the new proce-
15 dure, measurements were repeated over a period of 5 months. The detection subsystem stability was monitored from lidar profiles measured with a unique nitrogen filter used for detecting the signal in the two measurement channels. Compared to the previous campaign (Development of Methodologies for Water Vapor Measurement, Demevap), we observe an improvement in the stability of the system based on the nitrogen measurements which showed a drift of less than 3% per month
20 and a standard deviation of about 3% during the campaign. The water vapor calibration coefficients were determined from capacitive humidity sensor measurements and from GPS zenith wet delays measurements. They show a similar small drift of 3% per month and a standard deviation of $\sim 6\%$. Thanks to the N_2 measurements, the drift can be completely removed. Lower standard deviation can
25 be achieved by increasing the Signal to Noise Ratio and/or spatial and temporal integration window.

1 Introduction

The Raman lidar has become, after several decades of research and development, a privileged device for the measurement of atmospheric water vapor profiles. Its ability to measure small spatial and temporal scales of the water vapor field is of prime interest for weather forecasting and climate studies (Held and Soden, 2000). Water vapor plays a role in the climate feedback induced by radiative forcing which is still poorly understood even if it has been evidenced to be substantial (Soden et al., 2002). Moreover, water vapor Raman lidar provides to the Global Navigation Satellite System (GNSS) community a way to correct altimetry data using the wet path delays, which result from the presence of water vapor along the signal path through the atmosphere (Bosser et al., 2010). For this specific purpose, the Institut National de l'Information Géographique et Forestière (IGN) and the Laboratoire Atmosphères, Milieux, Observations Spatiales (LATMOS) have developed jointly the water vapor Raman lidar Rameau (Bock et al., 2001; Tarniewicz et al., 2002). The ability of the IGN Raman lidar to retrieve water vapor has been confirmed during several campaigns involving other instruments measuring the water vapor, and these good results led us to consider new applications for our lidar. High accuracy and stability of the retrieved data, which would be beneficial for climatological and meteorological studies, necessitate a careful and continuous calibration of the system. Indeed, calibration intends to get rid of absolute errors related to Raman cross sections, instrumental coefficients, and most of the atmospheric transmittance, and to correct for short-term and long-term instrument changes (Whiteman et al., 1992).

When it comes to lidar calibration, two approaches are usually considered: an independent and a dependent one. The former has been first described by Vaughan et al. (1988), who calculated the calibration coefficient as a combination of the H_2O and N_2 Raman backscatter cross sections from Penney and Lapp (1976) and the relative instrumental transmission from experimental measurements and manufacturer data. Later, Sherlock et al. (1999b) suggested a new method for the independent calibration, which aimed at monitoring drifts caused by system changes such as aging of optical components. This new method is based on the decomposition of the calibration coefficient in two terms, one is the transmission and detection efficiency of the Raman signals and is specific to each system and the other is the assessment of the Raman effective cross sections. Daytime measurements of diffuse sunlight are performed in order to determine the transmission and detection efficiency of the system. The Raman effective cross sections are estimated from semi-empirical models which take into account the temperature dependency of the Raman cross section. The effective cross sections are then convoluted with the instrument function. The absolute accuracy of this method is not better than 10%, mainly due to the uncertainties on the Raman cross section. So, to improve the determination of the calibration function, it is common to make use of an external source of water vapor mixing ratio (WVMR) measurement. The so-called dependent calibration method is thus performed by calculating a normalization factor from the comparison of the lidar profile with ei-

ther a radiosounding (Ferrare et al., 1995; Leblanc et al., 2011), or integrated water vapor (IWV) measurements from GPS, or microwave radiometers (Turner and Goldsmith, 1999), or ground based
65   humidity sensor data (Revercomb et al., 2003). The dependent method does not require to determine terms subject to large uncertainties such as the Raman cross sections of H_2O and N_2. The expected accuracy of this method is however limited by systematic and random errors in the lidar measurements and by the accuracy of the instrument/data chosen as the reference, that is 5% for radiosonde data, 2% for capacitive sensors, and 2-5% for GPS IWV data (Bock et al., 2013). The dependent
70   calibration method may not be convenient to monitor short-term variations in the system calibration coefficient (e.g. variations due to changes in optical alignment) or even long-term variations if the reference system is subject to changes. Hence, a combination of dependent and independent measurements is a good option to achieve better absolute calibration and a good stability.

Monitoring the short-term calibration variations is possible with specific measurements performed
75   between successive absolute calibrations. Sherlock et al. (1999b) suggest to control the calibration stability with background measurements and laser off during daytime, however this method is based on the need of independent aerosols data which limits its implementation. Lately, Leblanc and McDermid (2008) developed a stability control procedure with calibrated spectral lamps. The stability of their method is really good, reaching a standard deviation of 2% of the calibration factor over more
80   than a year. It also has to be mentioned that this calibration protocol has been chosen as a reference for the Raman lidars within the NDACC (Network for the Detection of Atmospheric Composition Change).

A cross comparison of various calibration methods based on external water vapor measurement
85   was achieved during the Demevap campaign, conducted in 2011 at the Observatoire de Haute Provence (OHP). Four methods were implemented using (i) point measurements from capacitive humidity sensors, (ii) radiosonde upper air measurements, (iii) IWV measurements, and, (iv) the GPS-lidar coupling developed by Bosser et al. (2010). A more detailed description of the methods and the overall outcomes of the campaign have been presented in a previous paper (Bock et al., 2013). Despite
90   the accurate vertical profiling capacity of the lidar, significant variations of the calibration coefficient were observed during this experiment. At long-term, an overall drift of 15% over the 45 days of campaign has been noticed, as well as a 7% peak-to-peak variation in the calibration coefficient between methods. Besides, for one given method, short-term fluctuations of 5% were observed during one night. The long-term variation has been linked with two experimental incidents leading to the change
95   of the optical fiber coupling the telescope receiver to the optical system containing the narrow band filters and photomultiplier tubes (PMTs). This instrumental change implied a complete realignment of the receiving optics, and as a consequence a jump in the calibration coefficient. We hypothesized that a change in the beam size or position on the PMT photocathode produced a different signal strength. Indeed, spatial non-uniformity of PMT photocathode sensitivity is a problem which has

100 been known for some time with the works of Takhar (1967); Dos Santos et al. (1996); Simeonov et al. (1999); Freudenthaler (2004). Solutions have been provided, which consist in adding a diffuser in front of each PMT window (Simeonov et al., 1999) or in adding field lenses and a mirror tube (Freudenthaler, 2004). These solutions allow to focus and/or spread the beam evenly onto the surface photocathode. However, they come along with a signal loss that has been assessed by Simeonov

105 et al. (1999) to be up to 25%, which is detrimental to the detection sensitivity of the weak Raman signals. While seeking for the minimization of the PMTs effects, we noticed that the fiber could also play a noticeable role in the variation of the calibration coefficient because of the modes fluctuations at the output. The combination of a multi-mode fiber and PMTs appeared to be an important source of fluctuations in the calibration coefficient of the lidar system. The removal of the fiber can

110 be achieved by a complete re-design of the optical system (see for example Leblanc et al. (2011)). We did not consider this option, however. Indeed, the fiber is very convenient to isolate the detection part from the reception part of a system and it has a function of field stop to limit the collection of background light. The challenge is now to reduce the variations of the calibration coefficient in a system including these two elements. In this article, the variation sources altering the stability of our

115 Raman lidar system are reviewed. We present the approach to study and mitigate them. Then, we expose the results of our optimization. This work is specific to our particular system but we discuss the variation sources that could impact other systems. In a first section, the IGN-LATMOS Raman lidar system is described as well as its likely variation sources. The second section is dedicated to the optical modifications we have made to reduce evident variation sources. Then in a third section, we

120 come back to our list of variation sources and attempt to quantify them through various experiments. Finally, we present experimental evidence of overall improvements of the system stability.

2 Presentation of the IGN-LATMOS Raman lidar and inventory of the sources of instability

Figure 1 draws the set-up of the IGN-LATMOS Raman lidar as it had been used during the Demevap campaign (Bock et al., 2013). Below we discuss the likely signal and calibration variation sources at

125 each stage of the system.

The emission part is composed of a Quantel Brilliant frequency tripled Nd:YAG laser, transmitting pulses of ∼60-70 mJ at 354.7 nm with a repetition frequency of 20 Hz. The divergence is around 0.5 mrad with a pointing stability (short term jitter) of 0.075 mrad measured over 200 shots. Monitoring

130 the pointing stability over several hours has evidenced however a movement (beam wandering) of the beam centroid of 0.5 mrad. Nevertheless, this beam wandering as well as the short term jitter and the beam divergence are reduced with a 8.4 × beam expander. The laser beam is eventually sent out into the atmosphere coaxially with the receiving telescope through two deflecting mirrors. The beam expander allows also insuring eye safety of the system. The laser pulse energy is monitored
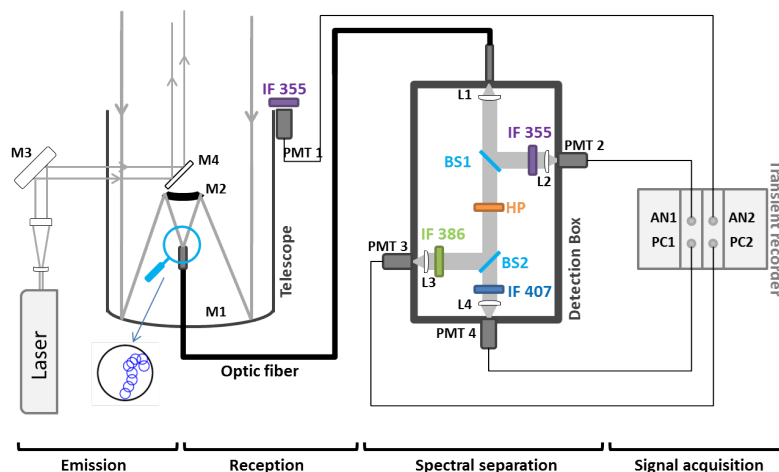
Figure 1. Schematic view of the IGN-LATMOS Raman lidar

135   by measuring a beam sample reflected by a thin glass plate with a Ophir laser energy meter and software on the main PC. Any significant variation in the energy is corrected by re-adjusting the alignment of the 3-ω crystal. There were only a couple of occasions when this alignment had to be re-adjusted during the Demevap campaign. Overall, the laser pulse energy fluctuations remained below 5%. The reception stage is composed of a 30-cm diameter 72-cm focal length Cassegrain

140   telescope coupled to the filtering and detection system with an optical fiber. During the first stage of Demevap, a 0.8 mm diameter optical fiber (Sedi Fibre, HCG800) was used. It was later replaced with a 0.4 mm diameter fiber (Sedi Fibre, TCG400). The field stop imposed by the fiber diameter limits the receiver's field of view to ± 0.27 mrad in the case of the 0.4 mm fiber. This is in principle large enough to contain the beam movements due to jitter and wandering of the transmitted beam.

145   Nevertheless, we observed during Demevap short-term fluctuations in the signal measured by PMT 2,3 and 4. These fluctuations were undoubtedly due to the spot sweeping off the fiber aperture, because neither the signal on the external channel nor the energy level recorded signal losses during the recording. Examples of two nights during which signal losses were recorded are shown on top of figure 2, where the signal on the N_2 channel is plotted in gray and signal on the H_2O channel is

150   plotted in black. On the bottom of figure 2, the ratio of the Raman signals is plotted together with the relative calibration coefficients computed from GPS ZWD. The signal break and fading observed on the Raman channels signals are most likely due to the spot sweeping off the fiber input. In addition, thermo-mechanical deformations of the optical bench are thus suspected to explain the spot movements and are currently investigated. In operation, the stability of the emission/reception alignment

155   is controlled by monitoring the signals. Hence, in case of signal fading, the transmitted laser beam is steered such as to maximize again the signal strength. Figure 2 shows also the calibration coefficients

variations. It seems thus that movements of the beam at fiber input cause changes in the alignment in the detection stage.
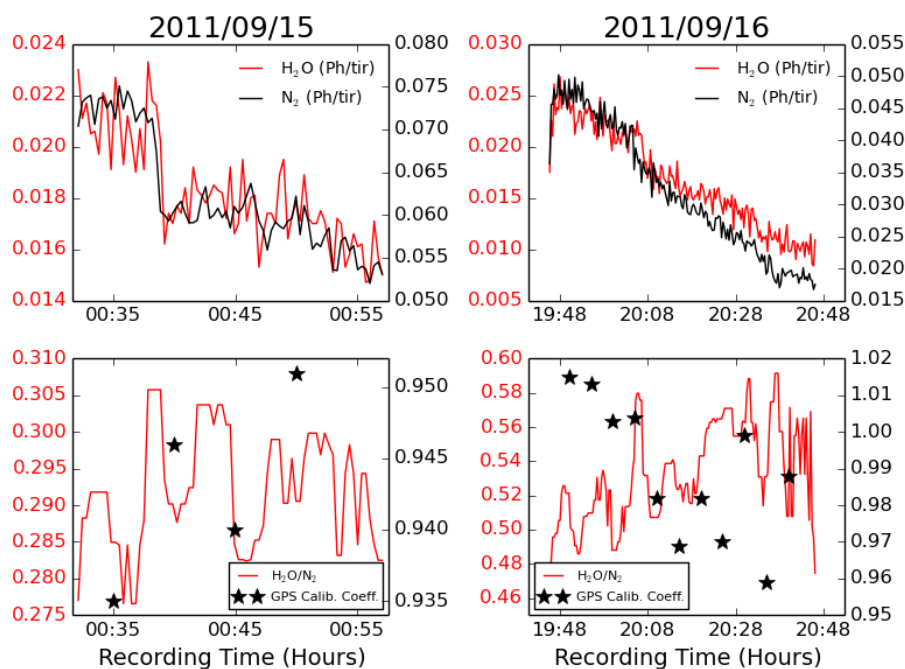
Figure 2. Examples of short-term instrument changes: signal break (left) and signal fading (right) on both Raman channels during the Demevap campaign. The top panels show N_2 photo-counts (grey) and H_2O photo-counts (black). The signals are given for the 317-1317 m layer and represent the number of recorded photons per laser shot. The bottom panels show the ratio of the two Raman channels (grey, smoothed) and the associated relative calibration coefficient computed from ZWD GPS data (black stars)

160   Multimode optical fibers are often thought as being optical signal scrambling devices but this is not really the case, especially for short fiber lengths. Short OH-rich fiber lengths are typically used in lidars to reduce signal loss and fluorescence (Sherlock et al., 1999a). The beam at the exit of such a fiber is composed of one or several superimposed modes. The output mode combination depends on the core diameter and numerical aperture of the fiber (Ghatak and Thyagarajan, 1989). Variations

165   at the input lead to variations of beam size and structure at the output which are detrimental to the stability of H_2O to N_2 signal ratio because of the spatial non-uniformity of the PMT. Figure 3 shows pictures of a sample of beam spots observed at the output of a 1-mm diameter fiber for various positions or tilts of a light source (468-nm LED) illuminating the fiber input with matched numerical

apertures ($NA_{in} = 0.22$). In addition to the changes in size and structure of the output beam, it was

170 also evidenced that the numerical aperture of the emerging beam can be larger than specified by the manufacturer. We tested Sedi Fibre fibers with diameters of 0.2, 0.4, 0.8, and 1.0 mm, which are all given for a NA = 0.22. For the larger fibers, 0.8 and 1.0 mm, we measured up to $NA_{out} = 0.30$. For the smaller fibers, 0.2 and 0.4 mm, the NA_{out} was consistent with the specifications. Another detrimental effect of a larger NA_{out} than assumed is vignetting on the lens or filters mounts or on the

175 PMT aperture (see next section). Variations in NA_{out} due to tilts of the incident beam or even tilts of the fiber core in its jacket have also been reported by Avila (1998). During the Demevap campaign, the change from a 0.8 mm fiber to a 0.4 mm fiber is suspected to be a major reason for a jump in the system calibration constant. The impact of changing fibers on the H_2O and N_2 signal ratio and thus the calibration constant is quantified in the next section.

180
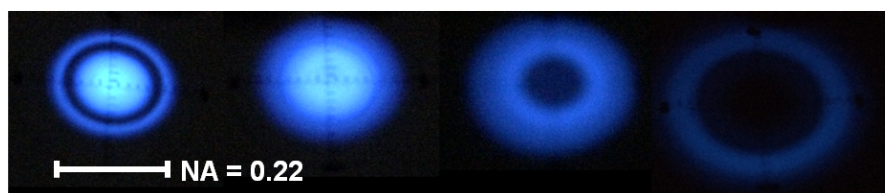
Figure 3. Screenshots of the output spot of a 1 mm diameter fiber illuminated with a blue diode for different incident angles. NA is the numerical aperture. The distance between the fiber and the screen is 20 mm.

The receiving module, for the filtering and the detection, is composed of a collimating lens L1 (focal length 46 mm), a series of two beam splitters (uncoated and coated UV-glass thin plates) B1 and B2, two high-pass filters (HP) to insure a rejection of the 354.7 nm signal to OD 12 (10^{-6} each), and narrow band interference filters (IF) to select either the Rayleigh/Mie (354.7 nm), Raman N_2

185 (386.7 nm) or Raman H_2O (407.6 nm) signals. Focusing lens L2, L3, and L4 (focal lengths 46 mm) are placed between the interference filters and the PMTs. The interference filters used during Demevap were from Barr Associates with bandwidths of 0.38 nm (H_2O), 0.44 nm (N_2) and 0.41 nm (Rayleigh/Mie). The filters were not intentionally tilted, so the incidence angles of the beams are assumed to be 0°. The temperature dependence of the Raman cross sections were hence computed

190 following Whiteman (2003), Avila et al. (1999, 2004) and Adam (2009). The vertical decrease of temperature between the surface and 10-km altitude is responsible for a 10% variation in transfer function of the H_2O filter. The temporal variation of the temperature profile during the Demevap campaign (September-October 2011) is responsible for a 3% variation in the altitude range 1-3 km. Corrections were applied to the measured WVMR profiles, in order to remove most of these vertical

195 and temporal variations. These corrections reduced the calibration coefficient drift observed during Demevap by 3% (Bock et al., 2013). However, variations in the incident angle and spatial structure

of the optical beam on the interference filters might also be responsible for small variations in the signal strengths. On the other hand, the temperature dependence effect on the filter characteristics are negligible. The PMTs used in the IGN Raman lidar are R7400-03 miniature metal channel dynodes

200 PMTs manufactured by Hamamatsu and assembled by Licel GmbH with a high-voltage divider. The PMTs are biased with individual stabilized high voltage (HV) power sources. However, it came out that due to thermal variations, the HV can fluctuate by a few volts around the nominal HV of 850 V. Tests with our PMTs revealed gain variations of ∼0.7% per volt. In order to avoid differential gain and calibration variations, the N_2 and H_2O PMTs are henceforth connected to the same HV

205 power supply. However, as we mentioned in the introduction, the major issue with PMTs regarding measurement stability is the spatial non-uniformity of their photocathode. The impact of this non-uniformity on the signal intensity differs from one PMT model to another. For example, Hamamatsu reports variations of ±10% for their R1387 series (Hamamatsu Photonics K.K., 2007), while Akgun et al. (2005) measure variations of less than 20% for the R7525HA. Simeonov et al. (1999) realized

210 a photocathode sensitivity map of PMTs from the Hamamatsu R5600 series (a previous release of Hamamatsu's miniatures PMTs), and reported variations from 0.2 to 2.8 times the mean signal value of the central part of the photocathode. These measurements have been recorded while scanning the 8 mm diameter PMT photocathode with a 200 μm light spot, which explains these substantial variations. In our system, the spot size is adjusted to be about half of the photocathode diameter, which

215 results in reducing the effects of the spatial non-uniformity of the PMT photocathode. Moreover, one can expect that the photocathode sensitivity got improved in the new version of these PMTs (R7400 series). A more detailed study of the sensibility of our PMT photocathode will be presented in section 4.1. The Raman signals are measured in photo-counting mode and the Rayleigh/Mie signals are measured in analog mode with a Licel GmbH transient recorder combining a 200 MHz counter and

220 a 12-bit 40 Ms/s analog digitizer.

3 Optical Optimization

The use of a large fiber (0.8 mm or 1 mm) has the advantage of larger receiver field of view (hence less sensibility to the beam wandering at input) but larger NA at the output. Examination of beam size in the receiving module revealed that vignetting was occurring on L1 and L2 due to larger than

225 expected NA. Figure 4 presents a ZEMAX® non-sequential ray tracing analysis of the nitrogen channel optical path. One can see on the upper panel the beam being cut by the first lens, evidencing that the vignetting effect inevitably happened during the first period of Demevap. Vignetting on L1, as well as on L3 or L4, lead to signal loss and affect the calibration coefficient, especially as the lengths of nitrogen and water vapor channels are not exactly the same. In order to eliminate

230 vignetting, we used the ZEMAX software to simulate and optimize the beam through the nitrogen channel path. The nitrogen channel has a longer optical path and is subjected to double reflection on

BS2, therefore the doubled spot on the PMT has more risk to be cut. In the simulation, the distances between L1 and L3 (457.5 mm) as well as between L3 and the PMT (32.25 mm) are set given the mechanical configuration of the optical detector unit. Besides, aperture sizes of the lenses have been

235 constrained considering the lens mounts. Double reflection on BS2 is accounted for assuming an axial shift of 0.75 mm from the optimal position. We tested different parameters such as the focal length of the lenses or the NA and diameters of the fibers seeking setups without vignetting. For each lens and fiber combination, the distance between the source –i.e. fiber output– and L1 is optimized with the software to obtain a collimated beam throughout the optical detector system. We came

240 out with two optimizations of the optical design of our receiving module allowing the complete transmission of the beam through the optical path and also the spreading of the spot over the PMT photocathode surface. We set 5 mm as a minimum for the spot diameter compared to the 8 mm of the photocathode. One option, presented in the middle panel of figure 4, is to choose a shorter focal length lens (f = 40 mm) at the entrance of the optical receiving module (L1) and a smaller diameter

245 fiber (0.4 mm). Because of the quite large length of the optical path, a shorter focal length for L1 is not enough to eliminate the vignetting if a large fiber is chosen. Nonetheless, the use of a large diameter fiber is preferred because of the beam wandering at fiber input. As it is not possible to use a large fiber with the initial size of the optical detector system, we explored a way to reduce the optical path length. We succeeded in finding a layout of the receiving module for tests without making

250 irreversible changes. The bottom panel of figure 4 illustrates the optimized optical configuration for the new layout. The signal from the output of the 1 mm diameter fiber is collimated with a 30 mm focal length lens and reaches L3 after 256.5 mm through the optical module. The focal lengths of the lens suggested here are somewhat arbitrary, and other configurations that meet the non vignetting condition are possible.

fibre	f_{L1}	d_{L1-L2}	f_{L2}
0.8	46	457.5	46
Demevap			
0.4	40	457.5	46
Opt 1			
1	30	256.5	46
Opt 2			
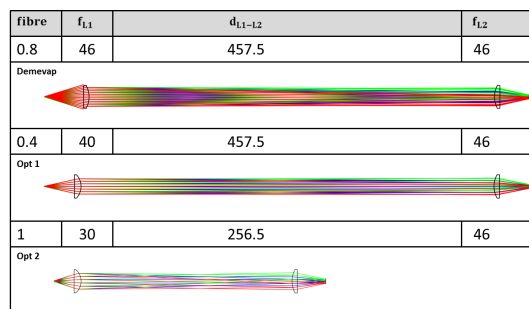
Figure 4. Optical path designs of the nitrogen channel : (top panel) during the first period of the Demevap campaign with a 0.8 mm diameter fiber - (middle panel) optimized keeping the original size of the detection module with a 0.4 mm diameter fiber - (bottom panel) optimized with a 1 mm diameter fiber and a reduced size optical path.

255   Finally, with these optimizations the adjustment tolerance of the fiber position with L1, found
theoretically with ZEMAX, is around 4 mm for the optimization 1 and 1.5 mm for the optimization
2. Because of its length and the double reflection on the beam splitter, the nitrogen Raman channel
constrains the interval. If the fiber is moved away from L1 the beam is cut on L2 and if, on the
contrary, the fiber is put closer to L1 there is vignetting on the PMT. The adjustment tolerance does

260   not mean a constant calibration coefficient on this range of position. It is thus important to note that
the calibration coefficient is likely to change between two campaigns or during experimental tests if
the fiber is repositioned or changed.

4   Quantification of the instability sources from laboratory measurements

Getting rid of the vignetting was a necessary preliminary task before studying other sources of vari-

265   ation. In this section, we will present the results of laboratory experiments conducted on the optical
detector system –separated from the rest of the system– in order to assess the impacts of the two
main sources introduced in section 2: (1) the spatial non-uniformity of the PMT photocathode and
(2) the spot movement on fiber input which implies both mode and numerical aperture fluctuations.
Both error sources are responsible for short and long term changes in the instrument response. Addi-

270   tionally, we also studied the impact of (3) the range-dependent spot size of the backscattered signal
on fiber input.
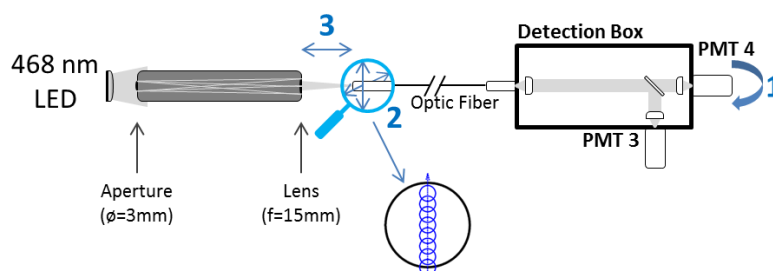
Figure 5. Overview of the experimental device composed by a light source (blue diode), a black aluminum tube
and a lens. The spot created is send to the receiving module through the fiber. Elements can be moved to assess
the impact on the measurements and calibration coefficient. (1) PMT Rotation for photocathode sensitivity test
(2) Spot translation to assess the laser beam wandering impact (3) Impact of the spot size on fiber input

An experimental device was designed to reproduce these variations in laboratory (the three insta-
bility sources investigated are symbolized by numbered arrows on figure 5) and estimate quantita-
tively their effects on the calibration coefficient, which here will be the ratio of the signal (photo-

275   counts) in water vapor and nitrogen channels $R_{43} = \frac{S_4}{S_3}$ with measurements made at the same wave-
length. The measured signal ratio can thus be expressed as: $R_{43} = \frac{T}{1-T} \cdot \frac{\eta_4}{\eta_3}$ where T is the transmis-

sion coefficient of BS2 and η_4 and η_3 the detection efficiency of channels 4 and 3, respectively, at the common wavelength.

The experimental device is presented in figure 5, the light source on the left enters a black aluminum tube across a pinhole of 3 mm. At the end of the tube, a lens and a diaphragm enable the light to focus on the fiber input. The focal length of the lens (15 mm) and the diaphragm size have been chosen so that the entering NA is similar to the one of the telescope (NA = 0.2). The diameter of the spot size on the fiber input has been calculated at 130 μm at 15.6 mm from the lens, thus the spot is supposed to be smaller than the diameter of the fiber. The distance adjustment of the fiber in front of the lens is crucial and an error of only 1 mm would lead to a spot about 4 to 5 times larger which cannot be acceptable for a 0.4 mm diameter fiber. The fiber is set on a micrometer 2-axis translation stage, which enables to move the spot position all over the surface of the fiber input. The fiber end is placed at the entrance of the receiving module. Each experiment is characterized by a combination of a choice of a fiber and lenses (L1/L3/L4) to test all the configurations mentioned in the previous section.

4.1 PMT photocathode spatial non-uniformity
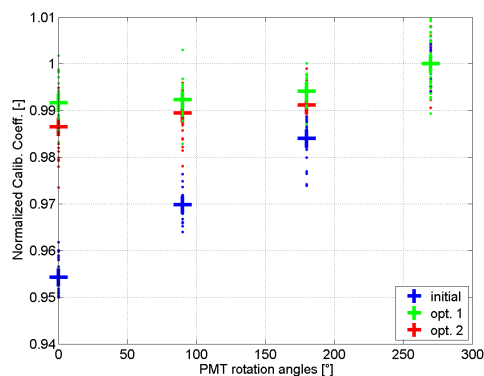
Figure 6. Variations of the normalized calibration coefficient with the PMT rotation angle for 3 optical configurations of the receiving module: (blue) initial configuration, i.e. first part of the Demevap campaign (green) optimization with the initial settings of the optical detection system (red) optimization with the reduced optical path.

The PMT key point is the spatial non-uniformity of the photocathode. Thus, to quantify its impact we monitored the calibration coefficient while rotating of the PMT (experiment n°1). The results are illustrated in figure 6, with the calibration coefficients recorded for four PMT rotation angles and for the three different optical configurations shown in figure 4. The blue points are related to initial optical configuration (large fiber diameter and long optical path). The maximal variation between

two positions is 4.6%. The green and red points are both associated with optimized optical configurations. The former corresponds to the combination of a small size fiber and a long optical path. It achieves an overall variation of less than 1%. The latter has been recorded using a large fiber and a reduced optical path, and gave us variations of 1.3%. The use of the optimized configuration shows significantly reduced variations.

4.2 Spot movement on fiber input
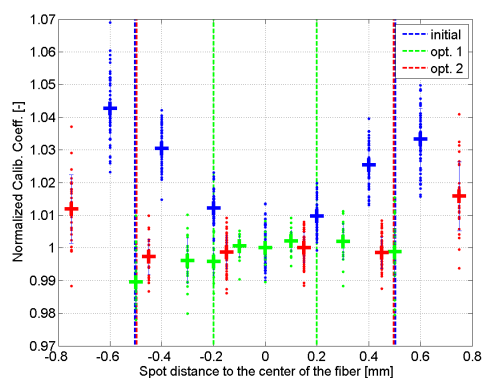
Figure 7. Normalized calibration coefficient variations for three optical configurations of the receiving module: (blue) during Demevap first part campaign (green) optimization with the initial settings of the optical detection system (red) optimization with the reduced optical path. The vertical dashed lines represent the edges of the fibers (the limit where less than half of the spot actually enters the fiber).

The second main point is to minimize the consequences of the spot movement on the fiber input caused by thermo-mechanical deformations of the optical bench. A way to reproduce the laser beam wandering was to displace vertically or horizontally the fiber in front of the tube (experiment n°2 on figure 5), thus the spot scans from side to side the entrance of the fiber. As it had been said above, the spot movement leads to mode fluctuations and results in changes in the beam pattern and size which imply variations of the calibration coefficient because of the spatial non-uniformity of the PMT photocathode. As for the experiment n°1, we performed the spot movement experiment on initial and optimized optical configuration of the receiving module. The results are exposed on figure 7 and we used similar colors for the different configurations that the ones in the previous figure. The vertical dashed lines represent for each configuration the size of the fiber, i.e. the limit beyond which less than half of the spot enters in the fiber. Measurements are possible outside the fiber diameter interval; however the signal is weaker because the spot size is at the edge of the fiber diameter and so less light passes through the fiber resulting in more noisy measurements. If we compare the respective variations of each configuration within these limits, the initial configuration (blue) shows variations

around 3.5% while optimized configurations record variations of about 0.5%. However, for measurements made beyond these limits, the variations can reach 1-2% for the optimized configurations.

4.3 Range dependence of the spot size

320   The two variation sources presented above can result from alignment and/or instrumental changes. The variation introduced in this section is due to the range dependence of the spot size at the fiber input and is then a source of range-dependent bias. Indeed, as it has been described in Jenness et al. (1997) if the fiber is placed at the infinity focus, the image of the smallest ranges is blurred and becomes bigger than the fiber under a certain distance. As a consequence of variation of spot size at

325   fiber input, variations in NA or beam modes at output are expected. The range dependence in signal strength due to PMT spatial non-uniformity was also studied by Simeonov et al. (1999). In their case, the spot does not grow but moves on the photocathode as a function of the range and this leads to variation in the signal strength. Hence, it seemed relevant to study this variation source and its impact on the calibration coefficient. For that purpose, the experiment n°3 on figure 5 has been performed

330   and consisted in moving away the fiber from the tube while recording the calibration coefficient. The spot light is adjusted to be at the center of the fiber, thanks to experiment n°2. This experiment has been tested on two configurations, the initial one (blue points) and the long optical path/small fiber optimized configuration (green points). Results are shown on figure 8. For both configurations, the effect of range dependence of the spot size is only a few tenths of a percent (0.7%). But, one

335   can notice that the results are much more scattered with the optimized configuration. This can be explained by the ratio of the spot size compared to the fiber diameter, as the spot on the fiber is growing the light is cut more rapidly by the fiber edges. This effect is negligible when all conditions are met for a properly aligned optical path in the receiving module.
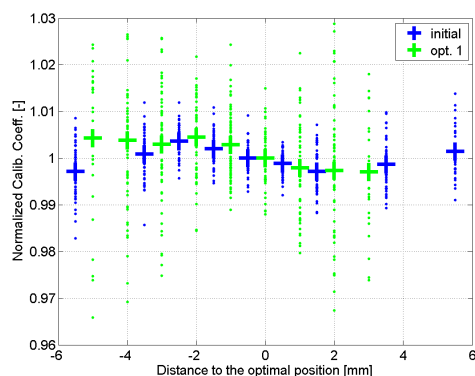
Figure 8. Influence of the size of the spot at the fiber input (blue) Demevap configuration (green) long optical path/small fiber configuration

5   Monitoring of instrumental stability during experimental campaign

340   The optimized configuration n°1 of the detection system has been implemented as well as several other improvements (cf. below), and the system was tested during a validation campaign at the IGN site of Saint-Mandé. It consisted of 14 nights of experimentations over 5 months, from March to July 2015 under clear sky conditions. The measurements were concentrated in several 5-minutes series and consisted in two types : (1) N_2 calibration monitoring and (2) H_2O measurements (see table 1).

345   The IGN Raman lidar was installed in a mobile small van equipped with a rooftop aperture through which the laser beam is transmitted. In addition, three GPS receivers (Trimble Net R9) associated with three PTU sensors (Vaisala PTU200, pressure, temperature and humidity) were installed on top of a building close to the lidar.

Compared to Demevap, several modifications were brought to the instrument:

350   - The first lens of the beam expander is controlled with a three axis micrometer positioning stage. On one hand, this allowed us to set the distance between the two lenses more precisely (Z-axis) and on the other hand it enabled to adjust easily a laser beam misalignment due to thermo-mechanical deformation of the optical bench (X-Y axis).

- The optimized configuration n°1 was setup: a 0.4 mm diameter fiber was chosen with the long

355   optical path. The optical configuration of the receiving module consisted of a shorter focal lens length at the entrance (f_{L_1} = 40 mm) and larger beam splitters. The other lenses (L2, L3 and L4) and the filters remained unchanged.

- More efforts were put on the adjustment of the optical elements throughout the optical path to avoid vignetting. This adjustment is performed by tracking the beam –formed by the light of

360   the blue LED– with different millimetric patterns.

- As for the electronic part, modifications have been made by Licel® to the transient recorder (change of the pre-amplifiers). We also decided to increase the photon detection threshold from 5 to 15 on the H_2O channel and from 5 to 20 on the N_2 channel, in this way, the detected photon rate matched properly the expected Poisson law and were not contaminated by spurious

365   noise signals.

- To avoid signal losses, as it had been seen on figure 2, recordings are limited to 5 minutes and the alignment adjustments of the laser beam are performed if signal level falls more than 10% of its initial value.

5.1   Water vapor profiles retrieval and calibration

370   The signals are acquired with a spatial resolution of 7.5 m and temporal resolution of 20 seconds (average over 400 laser shots). After background and saturation correction, the Raman signals are

Table 1. Summary of the lidar sessions during the campaign at Saint-Mandé. The numbers indicate the number of 5-minutes measurements of both types : H_2O refers to standard configuration and N_2 to measurements realized with a common nitrogen filter (See section 5.2 for further informations).

	12-Mar	7-Apr	9-Apr	14-Apr	22-Apr	11-May	12-May	03-Jun	06-Jul	15-Jul	30-Jul
H_2O	7	5	5	3	1	0	4	4	3	3	3
N_2	2	1	2	1	0	2	2	2	3	2	3

further averaged in 5-min time bins to improve their signal-to-noise ratio (SNR) and the WVMR is computed following the equation below (Whiteman et al., 1992):

$$r(z) = C_{lidar}(z) \frac{S_{H_2O}(z) - B_{H_2O}}{S_{N_2}(z) - B_{N_2}} \tag{1}$$

375 The determination of the calibration function $C_{lidar}(z)$ can be decomposed as follows :

$$C_{lidar}(z) = r_{N_2} \frac{M_{H_2O}}{M_{N_2}} \frac{C_{N_2}}{C_{H_2O}} \frac{T(z, \lambda_{N_2})}{T(z, \lambda_{H_2O})} \frac{\frac{d\sigma_{N_2}(z, \lambda_{N_2})}{d\Omega}}{\frac{d\sigma_{H_2O}(z, \lambda_{H_2O})}{d\Omega}} \tag{2}$$

where r_{N_2} is the mass mixing ratio of nitrogen, M_X the molecular weight of the species X, C_X the instrumental transmission and detection efficiency of the optical and electronic elements in the reception, spectral detection and signal acquisition elements of the system (see figure 1), $T(z, \lambda_X)$ the

380 atmospheric transmittance from ground to distance z at wavelength λ_X, and $\frac{d\sigma_X(z, \lambda_X)}{d\Omega}$ the Raman backscattering cross-section of the species X. The uncertainties associated with these three terms are typically 10% for instrumental coefficients (based on manufacturer informations and/or laboratory measurements, Tarniewicz et al. (2002)), 2–5% for the differential atmospheric transmission, depending on the aerosol content (Tarniewicz et al., 2002), and 10% for Raman cross sections (Pen-

385 ney and Lapp, 1976). For most applications, the calibration coefficient has to be determined with a higher accuracy (e.g. better than 5% for climate studies).

During our experimental campaign, the instrument stability was monitored through N_2 measurements and the absolute calibration of the system was achieved with two auxiliary WVMR measurements : zenith wet delays (ZWD) estimates from GPS data and humidity measurements from PTU

390 sensors. Note that calibration with IWV and ZWD data are completely equivalent (Bosser et al., 2010).

Figure 9 shows an example of the WVMR profile derived from the Raman lidar signals in Saint-Mandé (blue) as well as the radiosonde (in red) recorded in Trappes at about 30 km from Saint-Mandé. It has to be noted that the lidar profile is not calibrated, but the *a priori* calibration coefficient

395 has been implemented which explains the similar values of the two profiles. These non-collocated profiles do not agree all the time, especially when the atmosphere is highly variable. Thus, we did not use the radiosonde data at lower levels for the lidar calibration during the campaign. The height of the PTU sensors and the GPS receivers is 15 m above the lidar system which allows to have collocated lidar and PTU measurement for calibration and the ZWD computation does not need a complement
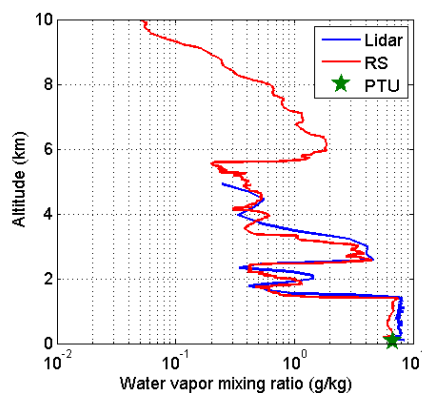
Figure 9. Vertical water vapor mixing ratio profiles measured by the IGN Raman lidar (blue) and a radiosonde (red). The radiosonde was launched at 30 km from the lidar. The PTU data at 15 m from the ground is also drawn in green.

400   in the lower layers. As for the upper layers, the lidar profile is completed with the radiosonde profile from Trappes from 5 to 10 km, beyond this altitude we use a standard atmospheric model but its contribution to ZWD is quite negligible given the lower quantity of water vapor at these altitudes.

The temporal variations of the PTU temperature and WVMR over the 5 months of campaign are shown in figure 10. The first nights are quite dry and can be associated with low SNR in the lidar
405   water vapor measurement.

5.2   System stability with N$_2$ calibration procedure

The control of the instrument stability is performed each night by means of measurements realized with a common nitrogen filter placed at the entrance of the receiving module, these measurements will be called "N$_2$ Calibrations" hereafter. For a reliable monitoring, we started and ended each night
410   by a 5-min recording session of "N$_2$ Calibration".

From these profiles we derived a coefficient calculated as a mean of the ratio of the signals measured on the H$_2$O and N$_2$ Raman channels on a selected layer. The choice of the layer is determined by a SNR higher than 10 which is reached between 150 and 800 m. Three different layers were compared: 150-250 m, 350-450 m and 850-950 m, the results of the calculation of the coefficients during
415   the Saint-Mandé campaign are shown on the left part of figure 11. We compared these results with the coefficients calculated, with the same method, during the Demevap campaign which is presented on the right part of figure 11. The normalized slopes and the dispersions are given in table 2.

Both time series show a drift towards larger values with time but as it can be seen in the column 4 of table 2, the important result here is to recognize that the slopes are much smaller (3×) for the
420   Saint-Mandé campaign. Note that the slopes obtained for the upper layer during Demevap are not
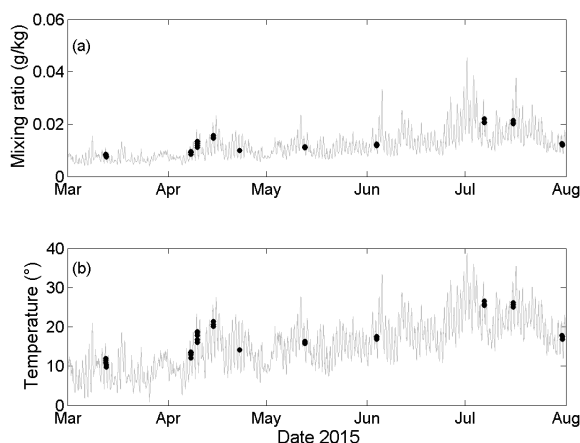
Figure 10. Time series of *(a)* the water vapor mixing ratio and *(b)* the temperature of the PTU for each lidar profile. The values are a mean of the PTU data over a 5-minutes period. The black dots indicate the Raman lidar WVMR profiles recording time.
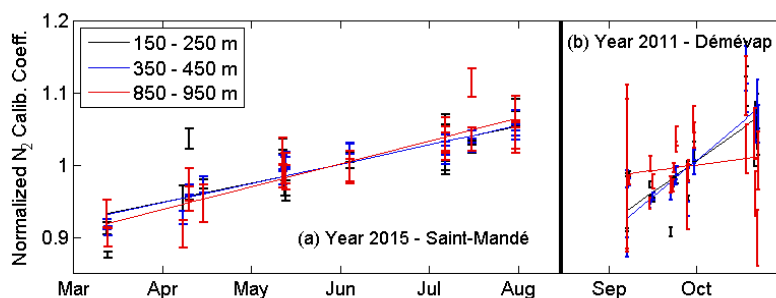
Figure 11. Time series of the mean of Raman signals ratio during measurements with a common N_2 filter during (a) Saint-Mandé campaign (b) Demevap campaign. Three different layers are considered : 150-250 m, 350-450 m and 850-950 m.

well determined due to lower SNR. This drift, which is not associated with the random process of laser beam drifts, is assumed to be partly caused by aging of the electronic components (10 year old PMT) and possible dust deposition on optics. Finally, the dispersion of the series (table 2, column 5), when the linear trend is removed, is as low as 1.6% for the Saint-Mandé campaign which is also a

425   significant improvement compare to Demevap. It shows that the short-term fluctuations in instrument response have been reduced.

Table 2. Comparison of the stability of the N_2 Calibration coefficients for the Saint-Mandé and Demevap campaigns on three different layers. The slope is estimated by a linear least squares regression. The last column represents the dispersion (standard deviation) obtained after removing the linear trend from the data.

		slope (%.month^{-1})	Dispersion (%)
	150-250 m	2.5 ± 1.4	3.1
Saint-Mandé	*350-450 m*	2.6 ± 0.73	1.6
	850-950 m	3.0 ± 1.1	2.3
	150-250 m	8.7 ± 1.5	3.4
Demevap	*350-450 m*	10 ± 1.1	2.6
	850-950 m	1.5 ± 1.9	4.4

5.3 Water Vapor Calibration with external measurements

During the Saint-Mandé campaign, the stability of the H_2O calibration coefficient (C_{lidar}) has been tested through two methods : the point humidity measurement matching from PTU capacitive sen-
430 sors (PTU method) and the GPS ZWD matching (GPS method). For each method, a set of parameters was examined in order to find the most stable time series of the lidar coefficient. For instance, for the PTU method different size and height of the layer used to compute the coefficient were tested. As for the GPS method, we sought the best way to complete the lidar profile in the upper layers testing different starting heights for the radiosonde. We chose the 67.5 m-height layer starting at 33.75 m
435 for the PTU method and for the GPS method we use the lidar profile up to 5 km, then the radiosonde profile from Trappes up to 10km and finally we used an empirical model for the highest layers. The final result is presented in the top panel of figure 12, on the left for the Saint-Mandé campaign and on the right for the Demevap campaign, where the PTU method is plotted in red and the GPS method in blue. The upper panel gives the relative calibration coefficient, that is the correction factor applied
440 to an a priori value for the absolute calibration coefficient. The bottom panel gives the normalized calibration coefficient, relative to the mean over the period. The points corresponding to the earlier nights of the Saint-Mandé campaign (March and April) are more scattered as a result of lower H_2O signals due to smaller atmospheric water vapor concentrations (see figure 10). The table 3 gives the dispersion of the coefficients and the slope of the linear regression estimated from the time series.
445 Similarly to the N_2 calibrations, one can see that there is a drift of 2-3% month^{-1} in the H_2O calibration coefficients. The important result here is to notice that the drift in the H_2O calibration coefficient is very consistent with the N_2 calibration results. As a consequence, it can be corrected within 0.5% month^{-1} (see last column of table 3). We chose the 350-450 m layer for the correction because of its better stability. Thus, we eliminate nearly the whole drift associated with the instrument response
450 change.

However, results reported in table 3 revealed that the dispersion was larger during the Saint-Mandé campaign (4-5%) compared to Demevap (2-3%). This is explained by the differences in measure-

ments set-up and subsequent quality of the used lidar data. During Demevap, two PTU sensors were installed on two 10 m masts at respectively 90 m and 180 m from the lidar system. Slant lidar profiles

455 were recorded in the direction of these sensors and the calibration coefficient was computed with a lidar point at a higher distance in the profile. As a result, the lidar data had a better SNR and were less subjected to electronic interferences usually found in the lower layers. As for the GPS methods, the lidar data used to compute the calibration coefficients during Demevap were integrated over a period up to 20 minutes which ensure higher SNR. Besides, the lidar profile was completed in the

460 upper layers with collocated radiosonde profiles launched twice a nigth, contrary to the Saint-Mandé campaign during which we used one non-collocated radiosonde profile per night. It is thus thought that with higher SNR on the lidar measurements, the dispersion of the H_2O calibration coefficients can be reduced to 2-3% as achieved during Demevap and extended vertical range.
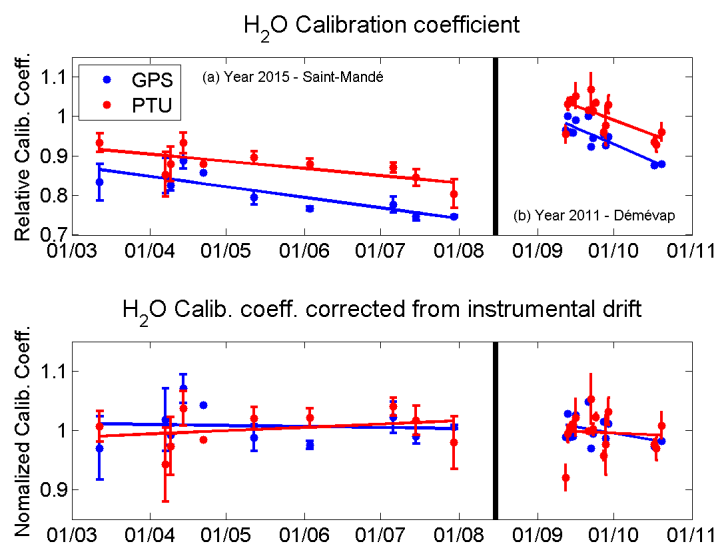
Figure 12. Top pannel: Time series of relative lidar calibration coefficients determined with the GPS method (blue) and the PTU method (red). Bottom pannel: Normalized calibration coefficients after the correction of the instrumental drift represented by the variations of the "N_2 calibration" coefficients for the 350-450 m. The results from the Saint-Mandé campaign are plotted on the left part and the results from the Demevap campaign on the right part.

Table 3. Comparison of the two H_2O calibration methods tested during Saint-Mandé campaign with (left) and without (right) correction of the drift based on linear regression of the N_2 calibration data.

	Method	No correction		After N_2 calibration drift correction	
		Slope (%.month^{-1})	Dispersion (%)	Slope (%.month^{-1})	Dispersion (%)
Saint-Mandé	PTU	-2.0 ± 0.08	5.7	0.48 ± 0.09	4.8
	ZWD	-2.8 ± 0.08	6.3	0.16 ± 0.09	4.4
Demevap	PTU	-10.5 ± 0.1	4.8	-3.6 ± 0.1	3.0
	ZWD	-8.8 ± 0.07	4.0	-2.1 ± 0.08	2.3

6   Conclusion and Discussion

465   We have presented a thorough study of the different instrumental instabilities found in our Raman
lidar system. Starting with the results of the last campaign, Demevap, we established a list of pos-
sible variation sources in instrumental response and calibration method. We showed that laser beam
wandering at the fiber input cause structure and size variations at the fiber output which imply dif-
ferential signal variations between the two Raman channels because of the spatial non-uniformity of
470   the PMT photocathode sensitivity.

Although each system has its own instrumental characteristics, the use of PMT for the photon
detection is very generalized in lidar system. In addition to the sensitivity variations of the pho-
tocathode, high voltage fluctuations –caused for instance by temperature fluctuations– may impact
their detection efficiency. As the laser beam wandering is inherent to the system and spot size vari-
475   ation with range is ineluctable, variations of the calibration coefficient can be expected. This will
automatically affect the stability of the measurement whether a fiber is used or not. In addition,
fluctuations of beam propagation modes are observed with a fiber.

We have shown that the short-term instrument response changes can be controlled within 1-2%
thanks to a rigorous alignment of the beam in the detection system (see section 4). The main source
480   of fluctuation is then beam wandering at the input of the fiber, which involves changes in the structure
and size of the beam at the output of the fiber. Optical optimization enabled to get rid of the beam
vignetting on optical elements, confirmed by laboratory tests which have shown a decrease from 10%
to about 1% of the variations associated with the spatial non-uniformity of the PMT photocathode.
Even if the optical optimization did not eliminate the issue of beam wandering, it has mitigated its
485   consequences from 3.5% to less than 1% during our tests.

An experimental campaign was implemented to assess the impacts of the modifications brought to
the system on its stability. On one hand, instrument stability was controlled with N_2 calibration mea-
surements and on other hand H_2O calibration coefficients of the WVMR profiles were determined
with PTU and GPS ZWD measurements. These results have been compared to the results obtained
490   during the Demevap campaign. We came out with a significant reduction of the drift observed in the

time series of H_2O calibration coefficients –2.0% per month for PTU method and 2.8% per month for GPS method– which represents a reduction by a factor of five with respect to Demevap results. Similar drifts were found in Brocard et al. (2013), where they observed a decrease of 1 to 5% per month in the WVMR lidar and radiosondes differences, and have been found to be caused by aging

495   components. However, aging could explain a part of the drift we observed but not all and we are left with long term non controlled variations. The drift observed on the H_2O calibration coefficients is correlated with the drift observed in the "N_2 calibration" coefficients. The latter can thus be used to correct the former. With the correction, the drift is almost totally removed.

The main problem of our lidar which could explain the drift, is the thermal expansion of the

500   optical bench which accentuates the amplitude of the spot movement. The thermalization and the strengthening of the lidar system frame is a priority for the future. Besides, a small-scale version of the optical detection system could be foreseen. In such small size system, the fiber would be removed and the receiving module would be placed right to the bottom of the telescope. Small size beam into the optic detection system would not be subjected to vignetting anymore. The reduced-

505   size of the receiving module would lead to the use of micro-sized PMTs that we expect to have a more homogeneous sensitivity of the photocathode.

Concerning the monitoring of the calibration stability based on the computation of daily "N_2 calibration" coefficients, it appeared to be quite easy to implement compared to the other techniques of calibration stability monitoring discussed in the introduction. Indeed, there is no need for auxiliary

510   aerosol measurements or stable spectral lamps and, contrary to the daytime measurement technique, we are able to get rid of the differential atmospheric transmission variations. However, the ratio is computed with measurements at the same wavelength and is not absolutely representative of the actual ratio of the optical transmission functions. Considering the very good results obtained with the hybrid calibration (Leblanc and McDermid, 2008), the partial calibration of our Raman lidar

515   could be improved by using a stable light directly at the entrance of the fiber, without going through the telescope. It would be quite easy to implement, given that our system is not equipped with extra telescopes, and in this way atmospheric content variability would not spoil the measurements.

Improving the accuracy and stability of the lidar measurements will also improve the positioning accuracy and stability of GNSS when the lidar ZWD measurements are used as calibration data. The

520   submillimetric level for the height estimation should be reached if we are able to provide ZWD data with an accuracy better than 3%. Furthermore, the willingness to open up the IGN Raman lidar to other research fields such as meteorology or climate studies, also requires an enhancement of the long term stability of our data.

Acknowledgements. The authors gratefully acknowledge Licel® GmbH for fixing the instrumental problems on

525   the transient recorder, and they also acknowledge the IGN-LOEMI staff (O. Martin, Y. Le Borgne) for participating to the nighttime measurements. This work was supported by the French national programme LEFE/INSU.

References

Adam, M.: Notes on Temperature-Dependent Lidar Equations, Journal of Atmospheric and Oceanic Technology, 26, 1021, doi:10.1175/2008JTECHA1206.1, 2009.

Akgun, U., Ayan, A. S., Bruecken, P., Duru, F., Gülmez, E., Mestvirishvilli, A., Miller, M., Olson, J., Onel, Y., and Schmidt, I.: Complete tests of 2000 Hamamatsu R7525HA phototubes for the CMS-HF Forward Calorimeter, Nuclear Instruments and Methods in Physics Research A, 550, 145–156, doi:10.1016/j.nima.2005.03.171, 2005.

Avila, G.: Results on Fiber Characterization at ESO, in: Fiber Optics in Astronomy III, edited by Arribas, S., Mediavilla, E., and Watson, F., vol. 152 of Astronomical Society of the Pacific Conference Series, p. 44, 1998.

Avila, G., Fernández, J. M., Maté, B., Tejeda, G., and Montero, S.: Ro-vibrational Raman Cross Sections of Water Vapor in the OH Stretching Region, Journal of Molecular Spectroscopy, 196, 77–92, doi:10.1006/jmsp.1999.7854, 1999.

Avila, G., Fernández, J. M., Tejeda, G., and Montero, S.: The Raman spectra and cross-sections of H_2O, D_2O, and HDO in the OH/OD stretching regions, Journal of Molecular Spectroscopy, 228, 38–65, doi:10.1016/j.jms.2004.06.012, 2004.

Bock, O., Tarniewicz, J., Thom, C., Pelon, J., and Kasser, M.: Study of external path delay correction techniques for high accuracy height determination with GPS, Physics and Chemistry of the Earth A, 26, 165–171, doi:10.1016/S1464-1895(01)00041-2, 2001.

Bock, O., Bosser, P., Bourcy, T., David, L., Goutail, F., Hoareau, C., Keckhut, P., Legain, D., Pazmino, A., Pelon, J., Pipis, K., Poujol, G., Sarkissian, A., Thom, C., Tournois, G., and Tzanos, D.: Accuracy assessment of water vapour measurements from in situ and remote sensing techniques during the DEMEVAP 2011 campaign at OHP, Atmospheric Measurement Techniques, 6, 2777–2802, doi:10.5194/amt-6-2777-2013, 2013.

Bosser, P., Bock, O., Thom, C., Pelon, J., and Willis, P.: A case study of using Raman lidar measurements in high-accuracy GPS applications, Journal of Geodesy, 84, 251–265, doi:10.1007/s00190-009-0362-x, 2010.

Brocard, E., Philipona, R., Haefele, A., Romanens, G., Mueller, A., Ruffieux, D., Simeonov, V., and Calpini, B.: Raman Lidar for Meteorological Observations, RALMO - Part 2: Validation of water vapor measurements, Atmospheric Measurement Techniques, 6, 1347–1358, doi:10.5194/amt-6-1347-2013, 2013.

Dos Santos, J. M. F., Veloso, J. F. C. A., Lopes, J. A. M., and Morgado, R. E.: A simple method to improve the spatial uniformity of venetian-blind photomultiplier tubes, IEEE Transactions on Nuclear Science, 43, 1335–1340, doi:10.1109/23.507061, 1996.

Ferrare, R. A., Melfi, S. H., Whiteman, D. N., Evans, K. D., Schmidlin, F. J., and Starr, D. O.: A Comparison of Water Vapor Measurements Made by Raman Lidar and Radiosondes, Journal of Atmospheric and Oceanic Technology, 12, 1177, doi:10.1175/1520-0426(1995)012<1177:ACOWVM>2.0.CO;2, 1995.

Freudenthaler, V.: Effects of Spatially Inhomogeneous Photomultiplier Sensitivity on LIDAR Signals and Remedies, in: 22nd Internation Laser Radar Conference (ILRC 2004), edited by Pappalardo, G. and Amodeo, A., pp. 37–40, 2004.

Ghatak, A. K. and Thyagarajan, K.: Optical Electronics, 1989.

Hamamatsu Photonics K.K.: Photomultiplier tubes, 2007.

Held, I. and Soden, B.: Water vapor feedback and global warming 1, Annual Review of Energy and the Environment, 25, 441–475, 2000.

Jenness, Jr., J. R., Lysak, Jr., D. B., and Philbrick, C. R.: Design of a lidar receiver with fiber-optic output, Applied Optics, 36, 4278–4284, doi:10.1364/AO.36.004278, 1997.

Leblanc, T. and McDermid, I. S.: Accuracy of Raman lidar water vapor calibration and its applicability to long-term measurements, Applied Optics, 47, 5592, doi:10.1364/AO.47.005592, 2008.

Leblanc, T., McDermid, I. S., and Walsh, T. D.: Ground-based water vapor Raman lidar measurements up to the upper troposphere and lower stratosphere - Part 2: Data analysis and calibration for long-term monitoring, Atmospheric Measurement Techniques Discussions, 4, 5111–5145, doi:10.5194/amtd-4-5111-2011, 2011.

Penney, C. M. and Lapp, M.: Raman-scattering cross sections for water vapor, Journal of the Optical Society of America (1917-1983), 66, 422–425, 1976.

Revercomb, H. E., Turner, D. D., Tobin, D. C., Knuteson, R. O., Feltz, W. F., Barnard, J., Bösenberg, J., Clough, S., Cook, D., Ferrare, R., Goldsmith, J., Gutman, S., Halthore, R., Lesht, B., Liljegren, J., Linné, H., Michalsky, J., Morris, V., Porch, W., Richardson, S., Schmid, B., Splitt, M., van Hove, T., Westwater, E., and Whiteman, D.: The Arm Program's Water Vapor Intensive Observation Periods., Bulletin of the American Meteorological Society, 84, 217–236, doi:10.1175/BAMS-84-2-217, 2003.

Sherlock, V., Garnier, A., Hauchecorne, A., and Keckhut, P.: Implementation and Validation of a Raman Lidar Measurement of Middle and Upper Tropospheric Water Vapor, Applied Optics, 38, 5838–5850, doi:10.1364/AO.38.005838, 1999a.

Sherlock, V., Hauchecorne, A., and Lenoble, J.: Methodology for the Independent Calibration of Raman Backscatter Water-Vapor Lidar Systems, Applied Optics, 38, 5816–5837, doi:10.1364/AO.38.005816, 1999b.

Simeonov, V., Larcheveque, G., Quaglia, P., van den Bergh, H., and Calpini, B.: Influence of the Photomultiplier Tube Spatial Uniformity on Lidar Signals, Applied Optics, 38, 5186–5190, doi:10.1364/AO.38.005186, 1999.

Soden, B. J., Wetherald, R. T., Stenchikov, G. L., and Robock, A.: Global Cooling After the Eruption of Mount Pinatubo: A Test of Climate Feedback by Water Vapor, Science, 296, 727–730, doi:10.1126/science.296.5568.727, 2002.

Takhar, P. S.: Resolution and Cathode Uniformity in Scintillation Counters, IEEE Transactions on Nuclear Science, 14, 438–442, doi:10.1109/TNS.1967.4324451, 1967.

Tarniewicz, J., Bock, O., Pelon, J., and Thom, C.: Raman lidar for external GPS path delay calibration devoted to high accuracy height determination, Physics and Chemistry of the Earth, 27, 329–333, doi:10.1016/S1474-7065(02)00008-6, 2002.

Turner, D. D. and Goldsmith, J. E. M.: Twenty-Four-Hour Raman Lidar Water Vapor Measurements during the Atmospheric Radiation Measurement Program's 1996 and 1997 Water Vapor Intensive Observation Periods, Journal of Atmospheric and Oceanic Technology, 16, 1062, doi:10.1175/1520-0426(1999)016<1062:TFHRLW>2.0.CO;2, 1999.

Vaughan, G., Wareing, D. P., Thomas, L., and Mitev, V.: Humidity measurements in the free troposphere using Raman backscatter, Quarterly Journal of the Royal Meteorological Society, 114, 1471–1484, doi:10.1002/qj.49711448406, 1988.

Whiteman, D. N.: Examination of the traditional Raman lidar technique. I. Evaluating the temperature-dependent lidar equations, Applied Optics, 42, 2571–2592, doi:10.1364/AO.42.002571, 2003.

Whiteman, D. N., Melfi, S. H., and Ferrare, R. A.: Raman lidar system for the measurement of water vapor and 610 aerosols in the earth's atmosphere, Applied Optics, 31, 3068–3082, doi:10.1364/AO.31.003068, 1992.